



# Modulating electronic structure of active sites on iron-based nanoparticles enhances peroxymonosulfate activation

Jun Xie<sup>a,b</sup>, Shaohua Wu<sup>a,\*</sup>, Caiyu Luo<sup>a,b</sup>, Juncong Zou<sup>a,b</sup>, Yan Lin<sup>b</sup>, Shanying He<sup>c</sup>, Chunping Yang<sup>a,b,d,\*\*</sup>

<sup>a</sup> Academy of Environmental and Resource Sciences, School of Environmental Science and Engineering, Guangdong University of Petrochemical Technology, Maoming, Guangdong 525000, China

<sup>b</sup> College of Environmental Science and Engineering, Hunan University and Key Laboratory of Environmental Biology and Pollution Control (Hunan University), Ministry of Education, Changsha, Hunan 410082, China

<sup>c</sup> College of Environmental Science and Engineering, Zhejiang Provincial Key Laboratory of Solid Waste Treatment and Recycling, Zhejiang Gongshang University, Hangzhou, Zhejiang 310012, China

<sup>d</sup> Key Laboratory of Jiangxi Province for Persistent Pollutants Control and Resources Recycle, Nanchang Hangkong University, Nanchang, Jiangxi 330063, China

## ARTICLE INFO

### Keywords:

Peroxymonosulfate activation  
High-valent iron-oxo species  
Singlet oxygen  
Heteroatom  
Advanced oxidation process

## ABSTRACT

Herein, iron-based nanoparticle catalysts with heteroatoms anchored on nitrogen-doped carbon layers were constructed and applied to peroxymonosulfate (PMS) activation for antibiotic degradation. Results showed that S doping was beneficial to PMS activation, while P doping reduced the activation efficiency. The S-doped catalysts achieved 100% removal of sulfamethoxazole (SMX) within 15 min with a normalized rate constant of  $130.4 \text{ min}^{-1} \text{ M}^{-1}$ . Electron paramagnetic resonance and scavenging tests proved that high-valent iron-oxo species (HV-Fe=O) and singlet oxygen ( $^1\text{O}_2$ ) mediated non-radical oxidation dominated the SMX degradation. Theoretical calculations and experiments elucidated that the electron-rich S atom donated electrons during PMS activation, which changed the valence state of Fe and enhanced the adsorption energy to PMS ( $E_{\text{ads}} = -11.219 \text{ eV}$ ), resulting in excellent catalytic activity. This work elucidated the effects of heteroatoms on the electronic structure of active site in nanoparticles and provided guidance for the development of advanced catalysts for PMS activation.

## 1. Introduction

To date, antibiotics have appeared in the aquatic environment in various ways due to the wide application of bactericidal drugs [1]. The resulting antibiotic pollution has become a worldwide environmental problem, and posed potential serious threats for human health due to its toxicity, biological tolerance, and persistence [2,3]. Sulfamethoxazole (SMX), a sulfanilamide antibiotic commonly used for bacterial infections, is present in natural water bodies because it cannot fully tackle in conventional wastewater treatment facilities [4,5]. Advanced oxidation process (AOPs) can quickly and efficiently degrade antibiotics into non-toxic or low-toxic products by generating a variety of highly oxidizing reactive species, which is considered to be one of the most effective ways to solve antibiotic pollution [6]. As one of the AOPs, the

catalyst-activated persulfate (PMS) system has become a research hot-spot because of its strong oxidation and environmental tolerance [7]. Among them, peroxymonosulfate (PMS) has been studied more because the electron distribution of its O-O bond is asymmetric compared to peroxydisulfate, making the O-O bond of PMS easier to be broken under the electron transfer of catalysts and thus to be activated easily to produce reactive species [8]. Moreover, PMS can produce more kinds of reactive species ( $\text{SO}_4^{\bullet-}$ ,  $\bullet\text{OH}$ ,  $\text{O}_2^{\bullet-}$ ,  $^1\text{O}_2$ , and high-valent metal-oxo species) than peroxydisulfate. These reactive species have different oxidation ability and selectivity, which can face a variety of wastewater needs [9]. Among these reactive species, the high-valent metal-oxo species and singlet oxygen ( $^1\text{O}_2$ ) mediated non-radical oxidation has the advantages of substrate specificity, anti-interference, and excellent pH adaptability, which is considered to be a potential technology to address antibiotic

\* Corresponding author.

\*\* Corresponding author at: Academy of Environmental and Resource Sciences, School of Environmental Science and Engineering, Guangdong University of Petrochemical Technology, Maoming, Guangdong 525000, China.

E-mail addresses: [wushaohua@hnu.edu.cn](mailto:wushaohua@hnu.edu.cn) (S. Wu), [yangc@hnu.edu.cn](mailto:yangc@hnu.edu.cn) (C. Yang).

<https://doi.org/10.1016/j.apcatb.2024.124138>

Received 1 February 2024; Received in revised form 23 March 2024; Accepted 27 April 2024

Available online 29 April 2024

0926-3373/© 2024 Elsevier B.V. All rights reserved.

pollution [10–12].

At present, it is very obvious that synthesis of good catalysts is important. Heterogeneous catalysts have the advantages of facile synthesis, high efficiency and low metal leaching, and can meet the above requirements more comprehensively. Wherein, iron nanoparticle/carrier composite catalysts have been studied and used frequently. Unfortunately, the O–O bond length in PMS is shorter than that in  $\text{H}_2\text{O}_2$ , which results in a higher activation energy barrier [13,14]. How to make the O–O bond break more easily at the metal active site has become the key to the efficient activation of PMS. Studies have shown that adjusting the electron density of metals is expected to shift the d-band center of metals upward and promote the interaction between metal sites and adsorbed molecules [15,16]. Hence, we hypothesized that manipulating the electronic structure of the metal active site might also enhance its binding ability with PMS, and ultimately promote the transfer of electrons from the metal to the peroxide bond to achieve efficient activation of PMS.

Heteroatoms modification can effectively change the electronic structure of active sites. Wang et al. demonstrated that oxygen doping can change the electronegativity of nearby carbon atoms from positive to negative [17]. The co-doping of iron and sulfur can also significantly change the charge density and distribution on the surface of g- $\text{C}_3\text{N}_4$  and enhance PMS activation [18]. Moreover, the kinetic activity of a single Fe- $\text{N}_4$  site can be regulated by controlling the electron-withdrawing/donating properties of the carbon plane through S doping [15]. It is thus speculated that the introduction of heteroatoms (P, S) with different electron-withdrawing/donating functions into the catalyst can effectively regulate the electronic structure of the transition metal. In addition, iron-based nanoparticles have been extensively studied for PMS activation. It has been proved that both the oxidation of S(II) and the reduction of Fe(III) exist in FeS [19]. The P element in  $\text{Fe}_2\text{P}$  has also been shown to promote iron circulation while activating PMS [20]. All these indicate the potential role of heteroatoms in iron-based nanoparticles. Based on the above discussion, it is necessary to systematically reveal the relationship between heteroatoms structure and performance regulation in iron-based nanoparticles by introducing heteroatoms (P and S) with different electronic structures, which has been less studied at present.

Herein, we designed a versatile strategy to systematically tune the electronic structure of Fe by integrating specific heteroatoms (S and P) into the iron-based nanoparticle catalysts that are stably anchored on nitrogen doped carbon layers. As a contrast, we also synthesized a heteroatom-free iron nanoparticle catalysts, which was modified on the basis of the previous method [21]. The synthesis steps, heteroatom doping level and Fe content of the three catalysts are almost the same. Meanwhile, we systematically studied the effects of the introduction of P and S on the structure, catalytic activity and distribution of reactive species, and further elucidated the mechanism of catalytic enhancement induced by heteroatom doping by means of characterization and density functional theory (DFT) calculations. In addition, we evaluated the application potential of the optimal-performing Fe@N/C-S catalysts. This work comprehensively elucidates the effect of heteroatoms (P, S) doping on the activation of PMS by Fe active sites, which provides a reference for regulating the electronic structure of active sites in nanoparticles to mediate the intrinsic activity of catalysts.

## 2. Materials and methods

### 2.1. Chemicals

Peroxymonosulfate (PMS,  $\geq 47\%$ ), methyl phenyl sulfoxide (PMSO,  $\geq 97\%$ ) and methyl phenyl sulfone (PMSO<sub>2</sub>,  $\geq 98\%$ ) were obtained from Sigma-Aldrich.  $\text{FeCl}_3 \cdot 6\text{H}_2\text{O}$ , phenanthroline, thiourea, melamine, phytic acid (70%), sulfamethoxazole (SMX), benzoic acid (BA), furfuryl alcohol (FFA), *p*-benzoquinone (*p*-BQ), nitrobenzene (NB), methanol (MeOH), tert-butanol (TBA), and sodium thiosulfate were obtained from

Sinopharm Chemical Reagent Co., Ltd. Milli-Q water was applied throughout all experiments.

### 2.2. Preparation of catalysts

In 20 mL ethanol, 0.183 g  $\text{FeCl}_3$  was added and stirred. After dissolution, 0.396 g phenanthroline was added to the solution with a stirring of 5 min. Then, 2.0 g melamine was added to the mixed solution as nitrogen source and carbon source, stirred at room temperature for 3 h, dried at  $80^\circ\text{C}$  for 2 h, and then transferred to a vacuum drying oven at  $80^\circ\text{C}$  for overnight. Under argon atmosphere, the dry powder was placed in a tube furnace in which temperature was increased to  $600^\circ\text{C}$  at a rate of  $5^\circ\text{C min}^{-1}$ , and then maintained for 2 h to allow the melamine to evolve into a nitrogen-doped carbon layer. The temperature was further increased to  $800^\circ\text{C}$  at the same rate at the same rate and then maintained for 2 h to further achieve the dispersion and encapsulation of the iron nanoparticles on the nitrogen-doped carbon layer. After the calcination, the black powder was obtained, which is composed of nitrogen-doped carbon layer loaded with a large number of iron nanoparticles, i.e., Fe@N/C. In order to remove excess metal particles, the obtained black powder was immersed in 1 M  $\text{H}_2\text{SO}_4$  solution for 15 h for purification, washed several times with Milli-Q water, and dried in vacuum at  $80^\circ\text{C}$  overnight.

Catalysts of Fe@N/C-S and Fe@N/C-P were prepared similarly as the synthesis process of Fe@N/C except that thiourea and phytic acid were chosen as the sources of S and P, respectively. The doping levels of P and S in Fe@N/C-P and Fe@N/C-S were identical by adjusting the amount of precursor. Specifically, we added 0.053 g phytic acid solution and 0.133 g thiourea after the dissolution of 0.183 g  $\text{FeCl}_3$  in 20 mL ethanol.

Fe-N/C catalyst was also prepared similarly as the synthesis process of Fe@N/C except that phenanthroline was not added.

### 2.3. Characterizations

The surface morphology of the samples was examined by field emission scanning electron microscopy (FE-SEM, Hitachi S4800) and transmission electron microscopy (TEM, TecnaiG2 F20, FEI). The XRD patterns were collected by a Rigaku SmartLab X-ray diffractometer with monochromatic  $\text{Cu K}\alpha$  radiation (40 kV, 40 mA). The specific surface area and pore size of the samples were determined by Micromeritics Tristar 3000 nitrogen adsorption-desorption isotherm. Before the measurement, the sample was pre-degassed at  $300^\circ\text{C}$  for 4 hours in vacuum. X-ray photoelectron spectroscopy (XPS) was performed on an ESCALAB 250 Xi photoelectron spectrometer equipped with an  $\text{AlK}\alpha$  x-ray source. Raman spectra were obtained by confocal micro-Raman spectrometer (Horiba Jobin Yvon LabRAM HR800) under 633 nm laser excitation. The signal of dominant active free radicals was studied by electron paramagnetic resonance (EPR, JES FA200).

### 2.4. Analytical methods

#### 2.4.1. DFT calculations

All DFT calculations were performed using MedeA-VASP. The calculation is based on density functional theory (DFT) and GGA-PBE exchange-related functionals to describe the interaction. Using the block Davidson (Normal) algorithm and the reciprocal space projection operator, the electronic iteration converges to  $1.0 \times 10^{-5}$  eV. 15 Å thick vacuum layers are set to avoid manual interaction. Since there is no magnetic moment in the model, the “normal” accuracy is used for non-magnetic calculation, and the default plane wave cutoff energy is 400 eV. For the simulation model, we constructed three crystal models of Fe (110),  $\text{Fe}_2\text{P}$  (111) and FeS (114) to study the interaction between carrier and active phase and electron transfer. The number of iron atoms in the three models is 72. The  $2 \times 2 \times 1$  k point Monkhorst filled grid is used to sample the integral of the Brillouin zone, and a denser grid ( $4 \times 4 \times 1$ ) is used to accurately determine the electron density.

The adsorption energy is calculated from  $E_{\text{ads}} = E_{\text{total}} - E_{\text{model}} - E_{\text{PMS}}$ , where  $E_{\text{total}}$ ,  $E_{\text{model}}$  and  $E_{\text{PMS}}$  are the total energy of the adsorption system, the energy of the model surface and the energy of the PMS molecule, respectively [22].

The charge density difference is calculated as  $\Delta\rho = \rho_{\text{AB}} - \rho_{\text{A}} - \rho_{\text{B}}$ , where  $\rho_{\text{A}}$  and  $\rho_{\text{B}}$  are the charge density of different monomers in the composite material, and  $\rho_{\text{AB}}$  is the charge density of the composite material [23].

#### 2.4.2. Kinetic model of SMX degradation

In all experiments, the degradation of SMX conforms to quasi-first-order kinetics, which can be described as:

$$\ln(c_t/c_0) = -k_{\text{obs}} \times t \quad (1)$$

where  $c_t$  is the concentration of SMX at a specific time  $t$ ;  $c_0$  is initial concentration of SMX;  $k_{\text{obs}}$  represents the apparent rate constant; and  $t$  represents reaction time (min).

The modified kinetic rate constant ( $k$ -value) for evaluating the SMX removal efficiency by various catalysts was described as followed:

$$k - \text{value} = \frac{k_{\text{obs}} \times c_{\text{pollutants}}}{c_{\text{PMS}} \times c_{\text{catalysts}}} \times \text{Removal efficiency}(\%) \quad (2)$$

Where  $k_{\text{obs}}$  is the observed reaction rate constant ( $\text{min}^{-1}$ ), and  $c_{\text{PMS}}$ ,  $c_{\text{catalysts}}$ , and  $c_{\text{pollutants}}$  are the concentration of PMS (mM), the catalyst ( $\text{g L}^{-1}$ ) and pollutants ( $\text{mg L}^{-1}$ ), respectively.  $k_{\text{obs}}$  normalized by the concentration of PMS, catalyst and pollutants could comprehensively show the capacity of PMS usage by catalyst per mass and enhance the comparability between different catalysts.

Other minor analytical methods are presented in the [supplementary information](#). Such as the concentration determination of organic pollutants and electrochemical testing were detailed in Text S1. The concentration calculation of reactive species was shown in Text S2.

### 2.5. Degradation experiments

The catalytic degradation experiment was performed in a 250 mL beaker containing 100 mL of SMX solution ( $10 \text{ mg L}^{-1}$ ), PMS (0.5 mM) and catalyst (0.05 g/L). Shaking at 800 rpm at  $25^\circ\text{C}$ . The initial pH of the solution was adjusted to 7.4 using borate buffer (2.0 mM). The catalyst was added to the SMX solution and stirred for 30 min to achieve the adsorption-desorption equilibrium, and then PMS was added to initiate the catalytic reaction. At various time intervals, 1 mL of sample was taken, filtered through a  $0.22 \mu\text{m}$  PTFE filter membrane, and quenched with sodium thiosulfate solution ( $15 \mu\text{L}$ , 1.0 M) for subsequent analysis.

In the cycle experiment, the catalyst was separated and washed several times with deionized water and ethanol, respectively, and then dried overnight at  $80^\circ\text{C}$  for the next cycle. The thermal activation of Fe@N/C-S was carried out in a tube furnace under argon atmosphere at  $350^\circ\text{C}$  for 1 h.

## 3. Results and discussion

### 3.1. Characterizations of catalysts

According to the SEM images, the synthesized Fe@N/C, Fe@N/C-P, and Fe@N/C-S catalysts were all composed of numerous crumpled layers loaded with particles, which was attributed to the same melamine precursor and calcination conditions (Fig. S1). Combined with elemental mappings and the structural changes of melamine during calcination, these three-dimensional thin crumpled layers are considered to be nitrogen-doped carbon layers with a size of about  $20\text{--}50 \mu\text{m}^2$  [21]. In addition, it also can be seen from the SEM images that the morphology of the three catalysts were different, and the EDS mapping confirms the successful introducing of P and S. We further studied the

internal structure of the catalyst by TEM and HRTEM images. As shown in Fig. 1a-c, in all three catalysts, the nitrogen-doped carbon layer firmly fixed and dispersed the nanoparticles (NPs) supported on it. The nanoparticles diameters of the Fe@N/C, Fe@N/C-P and Fe@N/C-S catalysts are about 10–15 nm, 50–100 nm and 5–10 nm, respectively. They have different sizes, which may be attributed to the different complexing abilities of phytic acid and thiourea (precursors of P and S) introduced during synthesis. Both phytic acid and thiourea can chelate iron ions and introduce heteroatoms during catalyst preparation, but phytic acid with six phosphate groups has stronger complexation ability, resulting in more iron and P aggregation and forming larger size  $\text{Fe}_2\text{P}$  nanoparticles during calcination. In contrast, thiourea with two amino groups had a more suitable complexation capacity to promote the formation of smaller FeS nanoparticles. Moreover, the particles on the surface of Fe@N/C-S material are smaller and more dispersed, which means that there may be more active sites exposed. Through lattice fringe analysis (Fig. 1d-f), it was found that the Fe NPs in Fe@N/C and Fe@N/C-S were wrapped with graphite carbon layers (0.335 nm and 0.334 nm). In addition, the lattice fringe spacing of the three NPs are different, which implied that they belong to different types of Fe NPs.

The type of NPs was further analyzed by X-ray diffraction (XRD). Fig. 1g shows the XRD patterns of the three catalysts. the peaks located at  $26.6^\circ$  of Fe@N/C and Fe@N/C-S can be indexed to the (002) phase in graphite, which is consistent with the results of HRTEM images. The XRD peaks of Fe@N/C at  $41.5^\circ$ ,  $43.9^\circ$ ,  $44.6^\circ$ , and  $65^\circ$  are identical to Fe (JCPDS #99-0064). The diffraction peaks of the P-doped catalyst at  $40.3^\circ$ ,  $44.2^\circ$ ,  $47.3^\circ$ ,  $53^\circ$ ,  $54.1^\circ$ , and  $73.6^\circ$  assign to  $\text{Fe}_2\text{P}$  (JCPDS #51-0943). Meanwhile, the diffraction peak of Fe@N/C-S at  $44.7^\circ$  is considered to be FeS (JCPDS # 37-0477), and it was wide and unclear, which may be due to the small particle size and high dispersion of Fe NPs, resulting in the passivation of the lattice structure [19,24]. In order to further prove that the diffraction peak is not the (101) phase in graphite, an S-doped catalyst without Fe was synthesized. It can be seen from Fig. S2 that the peak here belongs to FeS. Raman spectra also show that heteroatom doping can change the carbon structure and defect degree, and the  $I_{\text{D}}/I_{\text{G}}$  of the catalyst after S doping was significantly increased, which also implies higher catalytic activity (Fig. 1h).

X-ray photoelectron spectroscopy (XPS) spectra were applied to investigate the surface chemical properties of catalysts. Compared with Fe@N/C, the signal peaks of P and S appeared in the full-spectrum scans of Fe@N/C-P and Fe@N/C-S, respectively, confirming the successful doping of P and S (Fig. S3 and Table S2). ICP-OES also verified that the doping amounts of heteroatoms in the catalyst was consistent, which ensured the independence of exploring the influence of P and S elements on iron sites (Table S3). The high-resolution spectra of P 2p show two spin splitting peaks at 129.39 eV and 130.34 eV, respectively, corresponding to Fe-P [25]. At the same time, Fe-S also appeared at 162.63 eV and 163.93 eV in the S 2p spectrum [26], which confirmed the presence of  $\text{Fe}_2\text{P}$  and FeS in Fe@N/C-P and Fe@N/C-S, respectively (Fig. 2a and b). In addition, the position and area of Fe-P and Fe-S peaks in the P 2p and S 2p spectra of the catalyst changed after reaction, indicating that P and S played a critical role in the activation of PMS. XPS Fe 2p spectra of catalysts were also presented in Fig. 2c-e. Three catalysts have spin splitting peaks of  $\text{Fe}^{2+}$  and  $\text{Fe}^{3+}$ , and heteroatom doping leads to different peak positions and areas, among which Fe@N/C-S has the highest  $\text{Fe}^{2+}$  content, reaching 54.15% (Table S4). After the reaction, the values of  $\text{Fe}^{2+}/\text{Fe}^{3+}$  of the three catalysts were changed to varying degrees, indicating that the redox cycle between  $\text{Fe}^{2+}$  and  $\text{Fe}^{3+}$  was the key to activate PMS.

In XPS N 1 s spectra, all samples showed peaks of pyridine N, pyrrole N, and graphite N (Fig. 2f and Table S5). Among them, Fe@N/C-P has the lowest content of graphite N, while Fe@N/C-S has the highest content of graphite N, which is conducive to active PMS due to the promotion of electron transfer of N/C carriers [22,27]. In addition, we also note that compared with Fe@N/C, the graphite N of Fe@N/C-P moves 1.07 eV to the high energy band, and the graphite N of



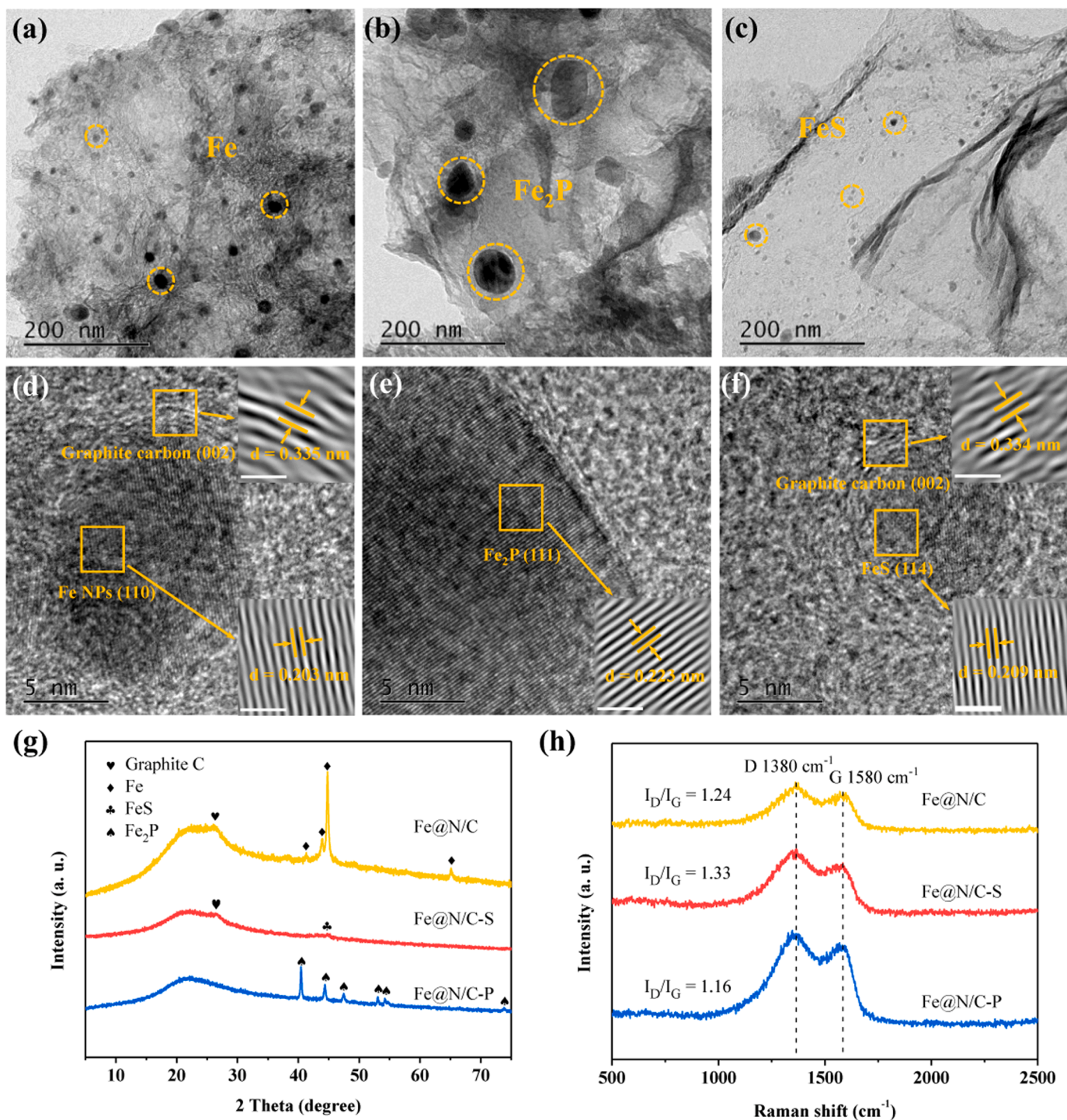


**Fig. 1.** Characterization of catalysts. (a-f) TEM and HRTEM images of Fe@N/C (a, d), Fe@N/C-P (b, e), and Fe@N/C-S (c, f); (g) XRD patterns of catalysts; (h) Raman spectra of catalysts.

Fe@N/C-S moves 1.68 eV to the low energy band. We speculate that this may be due to the influence of Fe, FeS and Fe<sub>2</sub>P nanoparticles on the electronic structure of the nitrogen dispersed around them. Because different kinds of nanoparticles have different charge density distributions, this will further affect the charge distribution of the 1 S orbital of N in the carrier, which will eventually lead to the corresponding binding energy change. The C1s spectra of Fe@N/C, Fe@N/C-P and Fe@N/C-S can be divided into four peaks: C-C (284.8 eV), C-N (285.92 eV), C=O (288.22 eV), and  $\pi$ - $\pi$  satellite, indicating that there are abundant functional groups in the catalysts (Fig. S4).

The specific surface area and pore structure of different heteroatom-doped catalysts were analyzed by N<sub>2</sub> adsorption-desorption isotherm (Fig. S5 and Table S6). The BET specific surface areas of Fe@N/C, Fe@N/C-P, and Fe@N/C-S were 336.0, 192.5, and 154.6 m<sup>2</sup>/g, respectively. It can be seen that the BET specific surface area decreases after the introduction of heteroatoms, which may be due to the formation of large-sized Fe<sub>2</sub>P NPs in Fe@N/C-P, leading to the collapse of the internal structure, while Fe@N/C-S formed more small dispersed FeS NPs, resulting in some micropores being occupied [28]. All three samples showed type IV isotherm and hysteresis loops (H3), signifying that



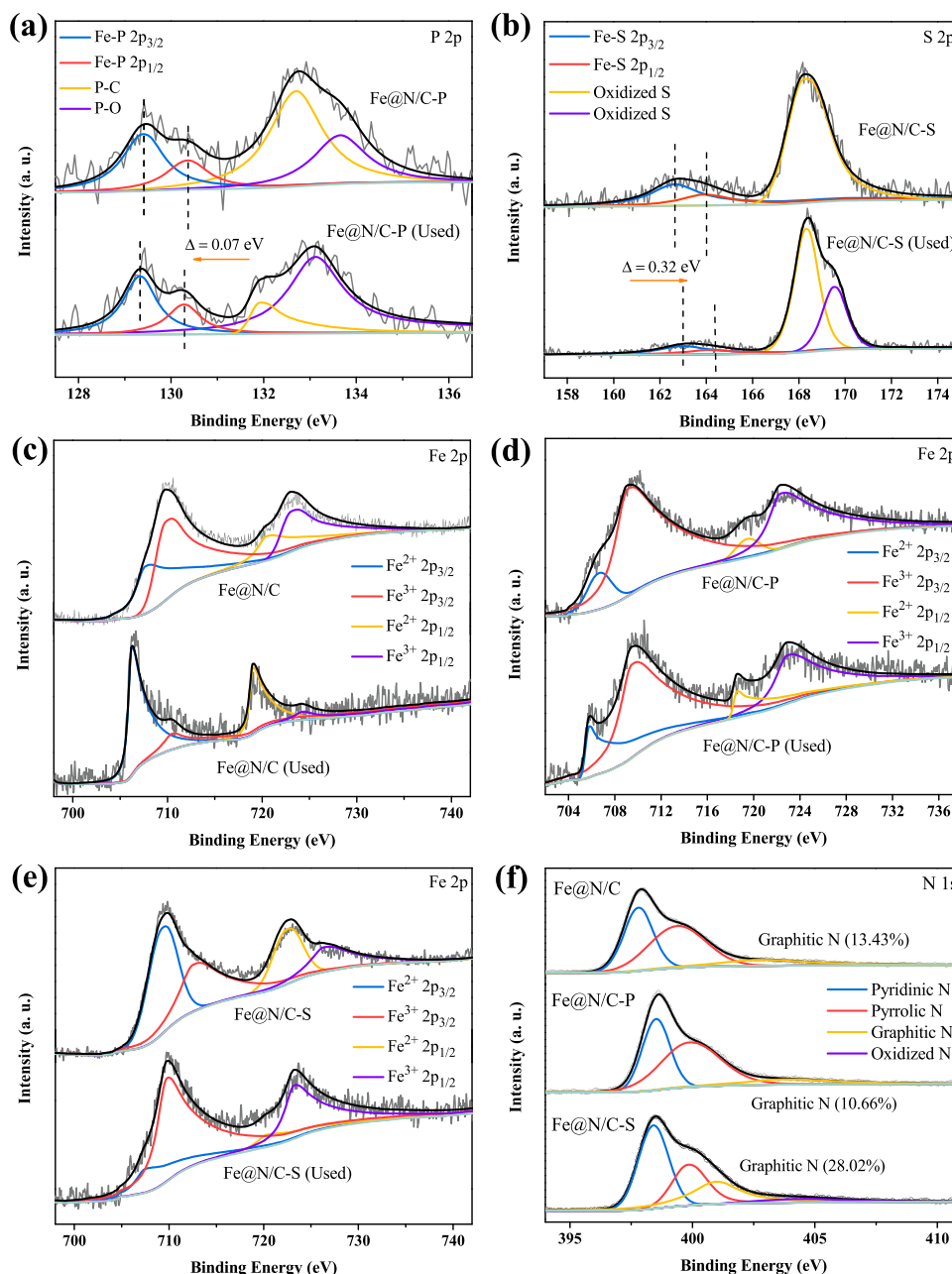


**Fig. 2.** High-resolution XPS spectra of catalysts. (a) XPS P 2p spectra of fresh and used Fe@N/C-P; (b) XPS S 2p spectra of fresh and used Fe@N/C-S; (c-e) XPS Fe 2p spectra of fresh and used Fe@N/C, Fe@N/C-P, and Fe@N/C-S; (f) XPS N 1s spectra of different catalysts.

there were more mesoporous (2–50 nm) and macroporous (>50 nm) structures.

### 3.2. Regulation of activation ability of PMS by heteroatoms doping

To assess the effect of heteroatom (P, S) induced electronic structure regulation of Fe centers on tuning PMS activation activity, we evaluated the catalytic performance for SMX removal. As shown in Fig. 3a and b, PMS can only remove 12% of SMX in 15 min without any catalyst. Before adding PMS, the highest removal rate of SMX by catalyst adsorption was only 16.5%. Notably, when PMS and catalyst exist simultaneously, the degradation performance of SMX is significantly improved, indicating that there is excellent synergistic interaction between them. Moreover, the catalysts doped with heteroatoms showed different degradation kinetics. Fe@N/C-S achieved complete removal of SMX within 15 min with a pseudo-first-order reaction rate constant of

$0.326 \text{ min}^{-1}$ , which was higher than Fe@N/C (95%,  $0.174 \text{ min}^{-1}$ ) and Fe@N/C-P (90%,  $0.134 \text{ min}^{-1}$ ), suggesting that the doping of P and S atoms with different electronic properties will affect the activation of PMS by iron active sites, and their effects are not consistent. In addition, we synthesized Fe-N/C without phenanthroline added to degrade SMX. Remarkably, the removal rate of SMX by Fe-N/C was 47%, and the  $k$  value was only  $0.01 \text{ min}^{-1}$ , which was much lower than that of other catalysts. It shows that phenanthroline can reduce the agglomeration of metal particles in calcination process well.

Furthermore, we also normalized the concentration of PMS, catalyst and pollutant with  $k$  value (named  $k$ -value), which can comprehensively reflect the ability of each mass catalyst to use PMS, and enhance the comparability between different catalysts (Eq. (2)). It is worth noting that the S-doped catalyst degraded SMX with a  $k$ -value of  $130.36 \text{ min}^{-1} \text{ M}^{-1}$ , showing the best catalytic performance among the recently reported advanced catalysts (Fig. 3c-d and Table S7), highlighting the

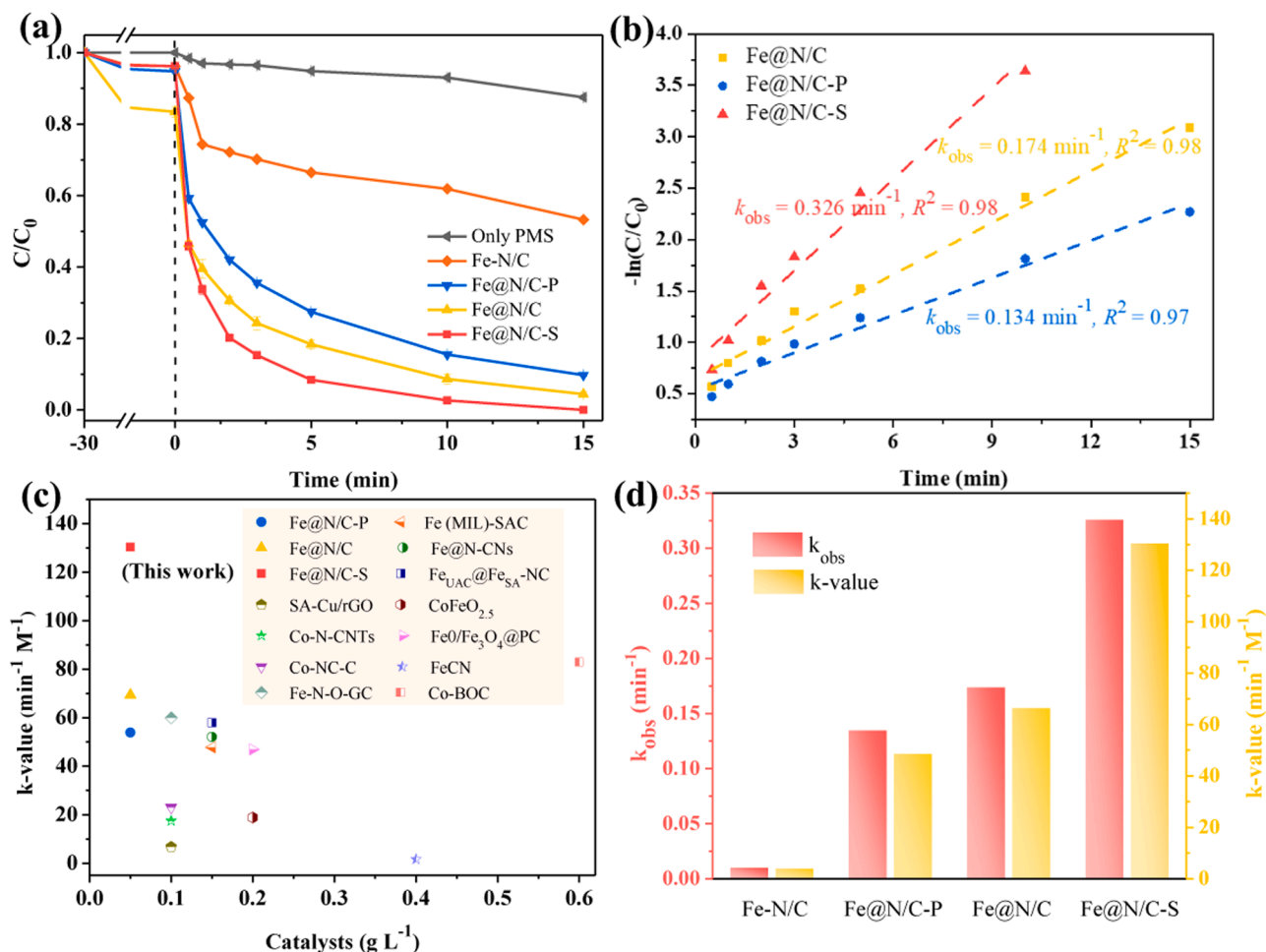


Fig. 3. Performances of SMX degradation in catalyst/PMS systems. (a) Effect of quenchers on SMX degradation; (b) Quasi-first-order kinetic model ling of SMX degradation data in catalyst/PMS systems; (c) Comparison of the kinetics of SMX degradation in recently reported catalysts; (d) Normalized  $k$  values of heteroatom-doped catalysts. Reaction conditions: [SMX] = 10 mg L<sup>-1</sup>, [PMS] = 0.5 mM, [catalysts] = 0.05 g L<sup>-1</sup>, T = 25 °C, and initial pH = 7.4.

superior catalytic performance of the S-decorated catalyst (Fe@N/C-S) for PMS activation.

### 3.3. Identification of reactive species and their contribution to SMX degradation

To explore the contribution of reactive oxygen species on SMX degradation, scavenging experiments and electron paramagnetic resonance (EPR) analysis were conducted. Tert-butanol (TBA, without  $\alpha$ -H) were selected as quenchers to capture  $\bullet\text{OH}$ . As displayed in Fig. 4a, excessive TBA only slightly inhibited the degradation of SMX in the three catalyst systems, indicating that there was only a small amount of  $\bullet\text{OH}$  in the system. EPR detected signals of DMPO- $\text{SO}_4^{\bullet-}$  and DMPO- $\bullet\text{OH}$ , qualitatively proving the presence of  $\text{SO}_4^{\bullet-}$  and  $\bullet\text{OH}$  in the three catalyst systems (Fig. S6). However, EPR analysis can only prove the presence of free radicals, not their contribution to SMX removal. Moreover, nitrobenzene (NB) and benzoic acid (BA) have high reactivity with  $\text{SO}_4^{\bullet-}$  and  $\bullet\text{OH}$ , so we further verified the contribution of free radicals in the system through probe experiments of NB and BA [29]. As shown in Fig. S7, NB and BA were almost not degraded, indicating that the role of  $\text{SO}_4^{\bullet-}$  and  $\bullet\text{OH}$  in the system are negligible, excluding their contribution.  $\text{O}_2^{\bullet-}$  is also a common free radical in PMS systems and is usually captured by  $p$ -BQ [30]. The presence of 2 mM  $p$ -BQ had a negative effect on SMX degradation, suggesting that  $\text{O}_2^{\bullet-}$  was one of the reactive species in the degradation process. However, studies have shown that  $\text{O}_2^{\bullet-}$  is usually present in PMS-based AOPs as  $^1\text{O}_2$  intermediates because of its low

reactivity to electron-rich organic pollutants [31]. This view was also verified in the following study. Under the same conditions, we added  $\text{O}_2^{\bullet-}$  quencher to perform EPR test, and found that the signal intensity of  $^1\text{O}_2$  was reduced to varying degrees, which means that  $\text{O}_2^{\bullet-}$  is the main intermediate for the formation of  $^1\text{O}_2$  (Fig. S8). In addition, the degradation of 1,3-diphenylisobenzofuran (DPBF), a specific probe of  $^1\text{O}_2$ , under  $\text{O}_2^{\bullet-}$  quencher was also observed to further verify the formation pathway of  $^1\text{O}_2$  [22]. As shown in Fig. S9, compared with the blank group, the degradation rate of DPBF in the presence of  $\text{O}_2^{\bullet-}$  quencher decreased by 25%, indicating that  $\text{O}_2^{\bullet-}$  was indeed involved in the formation of  $^1\text{O}_2$ .

In related studies, both FFA and L-histidine can be used as quenchers of  $^1\text{O}_2$ , and we experimentally verified that FFA consumes less PMS (Fig. S10). Therefore, we used FFA as the quench agent for  $^1\text{O}_2$ . It was found that under the co-existence of 5 mM FFA, the SMX degradation efficiency of Fe@N/C, Fe@N/C-P, and Fe@N/C-S decreased by 6.9%, 10.4%, and 16.1%, respectively. The results showed that  $^1\text{O}_2$  existed in all three systems, and the contribution of  $^1\text{O}_2$  to SMX degradation was different in the three systems. This was also confirmed by ESR analysis. TEMP- $^1\text{O}_2$  signals appeared in all three catalyst/PMS systems, and the signal intensity was consistent with the quenching effect of FFA (Fig. 4b). We further used the characteristic that  $^1\text{O}_2$  in  $\text{D}_2\text{O}$  has longer lifetime to verify the existence of  $^1\text{O}_2$ . As can be seen in Fig. S11, after replacing the solvent with  $\text{D}_2\text{O}$ , the degradation efficiency of Fe@N/C-S on SMX is further improved, which is consistent with the above experimental conclusions.

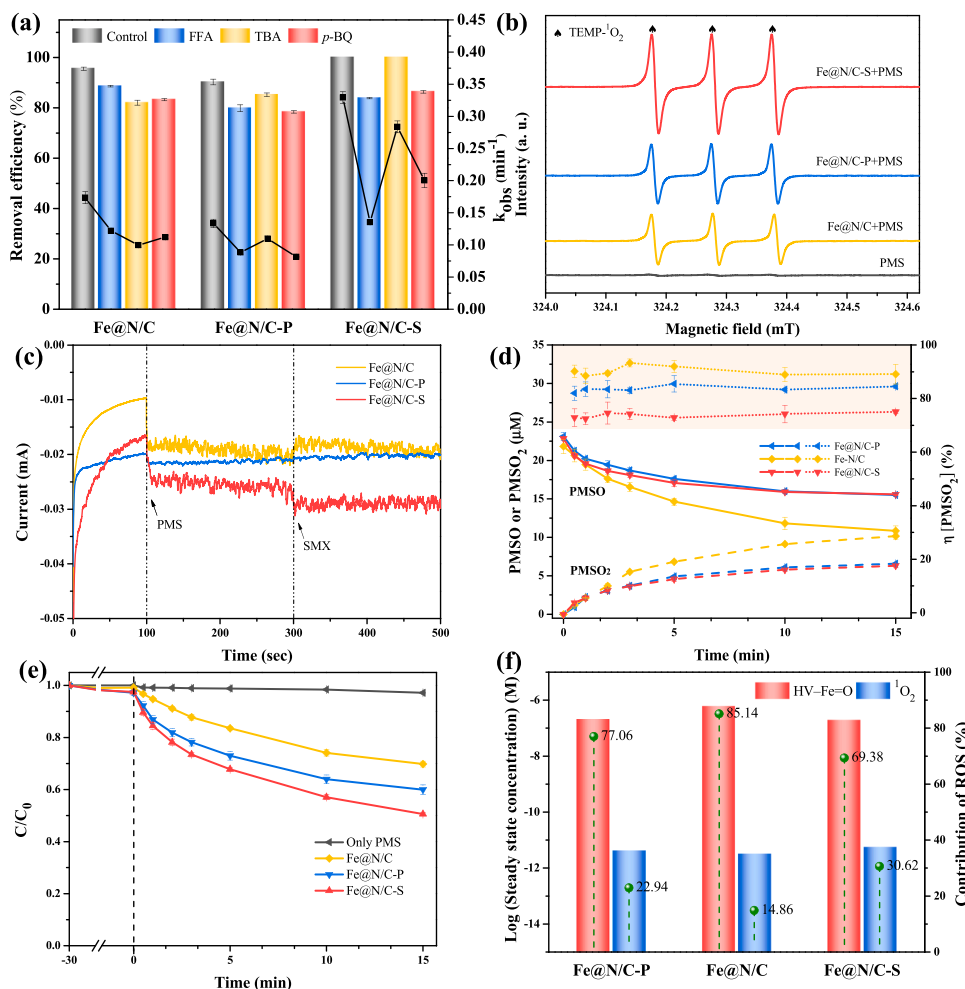


**Fig. 4.** Identification and of reactive species in PMS systems activated by different catalysts. (a) The effect of quenchers on the degradation of SMX in catalyst/PMS systems; (b) ESR spectra of  $^1\text{O}_2$  using TEMP as the capture agent at 3 min; (c) Dynamic current for different catalysts; (d) Conversion between PMSO and  $\text{PMSO}_2$  at catalyst/PMS systems; (e) FFA degradation in PMS systems activated by different catalysts; (f) Steady-state concentrations of HV-Fe=O and  $^1\text{O}_2$  and their contribution to SMX degradation. Reaction conditions:  $[\text{SMX}] = 10 \text{ mg L}^{-1}$ ,  $[\text{PMS}] = 0.5 \text{ mM}$ ,  $[\text{catalysts}] = 0.05 \text{ g L}^{-1}$ ,  $[\text{TBA}] = 500 \text{ mM}$ ,  $[\text{p-BQ}] = 2 \text{ mM}$ ,  $[\text{FFA}]_{\text{quenching agent}} = 5 \text{ mM}$ ,  $[\text{PMSO}] = 25 \text{ }\mu\text{M}$ ,  $[\text{FFA}]_{\text{probe}} = 10 \text{ mg L}^{-1}$ ,  $T = 25 \text{ }^\circ\text{C}$ , and initial pH = 7.4.

FFA could not completely inhibit the degradation of SMX, indicating that there are other reactive species in the system. We then used electrochemical tests to verify the possibility of electron transfer. In the i-t curve, the current intensity is significantly enhanced when PMS is added to a three-electrode system coated with catalyst (Fig. 4c). This phenomenon means that electron transfer occurs between the PMS and catalyst, causing the PMS to be activated by catalyst, resulting in a strong current fluctuation. Subsequently, SMX was continued to be injected to the electrolyte, and only slight current fluctuations occurred in the Fe@N/C-S and Fe@N/C electrochemical systems, indicating that these two catalysts had weak electron transfer with SMX, which confirmed that the electron transfer mechanism was not the dominant process. The experimental results of linear sweep voltammetry (LSV) also support the above conclusions (Fig. S12). Further, we monitored the change of PMS concentration in the pre-mixing stage of catalyst and PMS, and found that PMS was completely consumed by the catalyst within 30 min, which implied that the degradation efficiency of SMX would decrease with the prolongation of the pre-mixing time, and further demonstrated that the electron transport mechanism was not the dominant process (Fig. S13). Otherwise, the PMS will not be consumed by the catalyst at the pre-mixing stage, but only after the injection of SMX, they can achieve the consumption of PMS and degradation of SMX through the electron transfer mechanism. In conclusion, the above experimental results show that there is no electron transfer mechanism

in the three catalyst systems.

KSCN has a strong complexing ability with iron, and the formed chelate can hinder the accessibility of metal active sites, and are often used to determine the metal active sites in the catalyst [32]. When KSCN was added to the reaction system, the oxidation performance of SMX was significantly reduced, which proved that the high catalytic activity of the three catalysts was derived from the iron site (Fig. S14). In the study of PMS activation by iron-based catalysts, high-valent iron-oxo species (HV-Fe=O) have often been shown to contribute to the degradation of pollutants [12]. PMSO, which can be selectively oxidized to  $\text{PMSO}_2$  by high-valent metal-oxo species through the oxygen atom transfer reaction, was often used to demonstrate the role of HV-Fe=O [33]. We then used PMSO as the target pollutant to examine the contribution of HV-Fe=O. As shown in Fig. 4d, PMSO is oxidized to  $\text{PMSO}_2$  in all three systems, and its oxidation efficiency follows the order of  $\text{Fe@N/C} > \text{Fe@N/C-P} = \text{Fe@N/C-S}$ , suggesting that HV-Fe=O was the other main reactive species in the above systems. We further calculated the  $\text{PMSO}_2$  conversion rate ( $\eta_{\text{PMSO}_2}$ ) of the PMS systems activated by these three catalysts within 15 min (these three systems are simplified as Fe@N/C/PMS, Fe@N/C-S/PMS, and Fe@N/C-P/PMS, respectively.). It can be seen that the conversion rate of Fe@N/C/PMS system was about 90%, while the conversion rates of Fe@N/C-P/PMS and Fe@N/C-S/PMS system were 86% and 78%, respectively, both lower than the former. When PMSO is used as the quenching agent, it



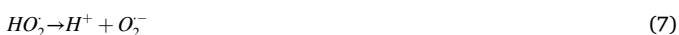
also has a strong inhibitory effect on the degradation of SMX (Fig. S15). These results show that HV-Fe=O was produced during the activation of PMS by all three catalysts.

In the previous discussion, we proved that Fe@N/C, Fe@N/C-P, and Fe@N/C-S activated PMS systems all generate  $^1\text{O}_2$  and HV-Fe=O. To further quantify their importance in the three catalyst/PMS systems, we evaluated the steady-state concentrations of  $^1\text{O}_2$  and HV-Fe=O and their contribution to SMX degradation through probe experiments of PMSO and FFA (Fig. 4d-e, Fig. S16, and Text S2). The equivalent steady-state concentration of HV-Fe=O in Fe@N/C/PMS system was  $0.627\ \mu\text{M L}^{-1}$ , 2.9 times and 3.2 times of that in Fe@N/C-P/PMS and Fe@N/C-S/PMS, respectively. The concentration of  $^1\text{O}_2$  is five orders of magnitude lower than that of HV-Fe=O, following the order Fe@N/C-S > Fe@N/C-P > Fe@N/C, which is different from the concentration distribution of HV-Fe=O (Fig. 4f and Table S8). However, the reactivity of HV-Fe=O for SMX is lower than that in  $^1\text{O}_2$ , and the concentration does not describe their contribution to the SMX degradation [34,35]. In this case, the contribution of HV-Fe=O and  $^1\text{O}_2$  to SMX degradation were calculated furtherly. As shown in Fig. 4f, HV-Fe=O played the major role in all three systems. The difference is that HV-Fe=O has the highest contribution rate in the Fe@N/C/PMS system, reaching 85.14%, while  $^1\text{O}_2$  has the highest contribution rate in the Fe@N/C-S/PMS system, reaching 30.62%.

To sum up, we can infer that HV-Fe=O and  $^1\text{O}_2$  were all present in the PMS systems activated by the three catalysts. However, due to the introduction of P and S, the valence distribution and electron density of Fe were different, which ultimately changed the concentration distribution of reactive species generated by catalyst activation of PMS. Moreover, the different reactivity of HV-Fe=O and  $^1\text{O}_2$  on SMX also leads to different degradation rates of SMX in the three systems.

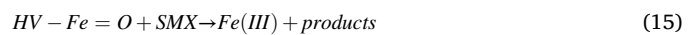
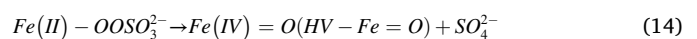
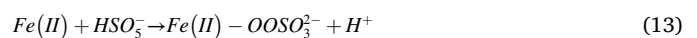
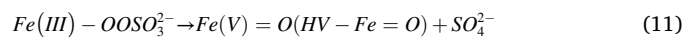
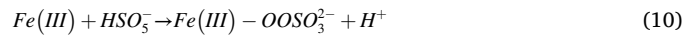
### 3.4. Activation mechanisms of PMS on catalysts

There are two theories about the formation mechanism of  $^1\text{O}_2$ . One is that the catalyst provides electrons, which breaks the peroxide bond of PMS and generates a variety of ROS. They react with each other to generate  $\text{O}_2^{\cdot-}$ , which is converted into  $^1\text{O}_2$  eventually. The other is that PMS provides electrons, generates  $\text{SO}_5^{\cdot-}$ , and then produces  $^1\text{O}_2$  through self-decomposition [11,36]. In the previous discussion, the existence of  $\text{O}_2^{\cdot-}$  in the system has been verified, indicating that  $^1\text{O}_2$  is likely to be generated through the intermediate  $\text{O}_2^{\cdot-}$ . We then used LSV analysis to verify the second mechanism. As shown in Fig. S12, the current density of the three catalyst systems did not increase after the addition of PMS and SMX in turn, indicating that PMS and SMX did not transfer electrons to the catalyst, excluding the possibility that PMS provided electrons to generate  $\text{SO}_5^{\cdot-}$  [22]. In addition, we also excluded the role of dissolved oxygen in the formation of  $^1\text{O}_2$  by argon purge experiments (Fig. S17). From the above analysis, it can be inferred that the production of  $^1\text{O}_2$  is derived from the mutual conversion of ROS, rather than the self-decomposition of  $\text{SO}_5^{\cdot-}$  (Eqs. (3)-(9)).



As for the generation of HV-Fe=O, it has been reported that it is

achieved through the catalysis of Fe(III) [37]. Fe(III) first binds to the hydroxyl O in PMS, and then undergoes proton dissociation and O-O bond cleavage to form HV-Fe=O (Eqs. (10)-(15)). We further shed light on the role of Fe(III) by analyzing the XPS Fe 2p spectra before and after the catalyst reaction. As shown in Fig. 2c-e, the  $\text{Fe}^{3+}$  content of Fe@N/C and Fe@N/C-P decreased by 30.19% and 9.5% respectively after the catalytic reaction, indicating that  $\text{Fe}^{3+}$  participated in the formation of HV-Fe=O. Meanwhile, the maximum decrease of  $\text{Fe}^{3+}$  at Fe@N/C/PMS system corresponds to the highest HV-Fe=O production. Of note, Fe@N/C-S showed an increase in  $\text{Fe}^{3+}$  content and a decrease in  $\text{Fe}^{2+}$  content after reaction. These results indicate that there was an activation mechanism in the Fe@N/C-S/PMS system, in which  $\text{Fe}^{2+}$  transfer electrons to PMS to generate ROS and then further evolve into  $^1\text{O}_2$ . According to the decrease of  $\text{Fe}^{2+}$  content in Fe@N/C-S/PMS system, it can be inferred that the activation mechanism was stronger than the other two catalyst/PMS systems, resulting in a higher concentration of  $^1\text{O}_2$  than the other two systems.



What roles do P and S play in the process of catalyst activation of PMS? We analyzed the XPS P 2p and S 2p spectra in depth. After the reaction, the binding energy of S 2p belonging to Fe-S increased by 0.32 eV, while the Fe-P of P 2p shift 0.07 eV toward the lower binding energy (Fig. 2a and b). The increase of the electron binding energy means a decrease of the electron density of the atom [38,39]. Therefore, the above XPS results show that doped S provided electrons to Fe during the activation of PMS, thus promoting the cycling between different valence states of iron, and finally achieving the improvement of catalytic activity [19,20]. On the contrary, the shift of Fe-P towards low binding energy proves that the doped P is electron-grabbing and slows down the electron transfer between the catalyst and PMS, which is not conducive to the activation of PMS. It is obvious that the XPS analysis results were completely consistent with the experimental phenomenon.

### 3.5. Modulating of electronic structure of iron active site by heteroatoms doping

To figure out the effect of P and S introducing for electron distribution on Fe active sites deeply, DFT calculations were used to shed light on the electronic structures in different adsorption configurations. In the three catalyst/PMS systems, the nitrogen doped carbon layers was consistent, and the active sites were mainly the crystals that supported on the layers. Therefore, we constructed the adsorption configurations of PMS with three different crystals. As shown in Fig. 5a, the O-O bonds of PMS were significantly broken after activation, indicating that PMS was successfully activated on the catalyst. According to relevant report, the electron transfer effect caused by heteroatoms doping will repel the d-orbitals of transition metals, thus increasing the d-orbital energy level [40]. We speculate that P and S with different electronic structure densities will affect the position of the d-band center when they bind to the iron site, respectively. It can be seen from the projected densities of state (PDOS) of the three catalysts that the doping of P and S significantly affects the electron density distribution of the Fe 3d orbital. Further calculations show that the introduction of P reduces the d-band center of the iron site, while the doping of S increases the d-band center

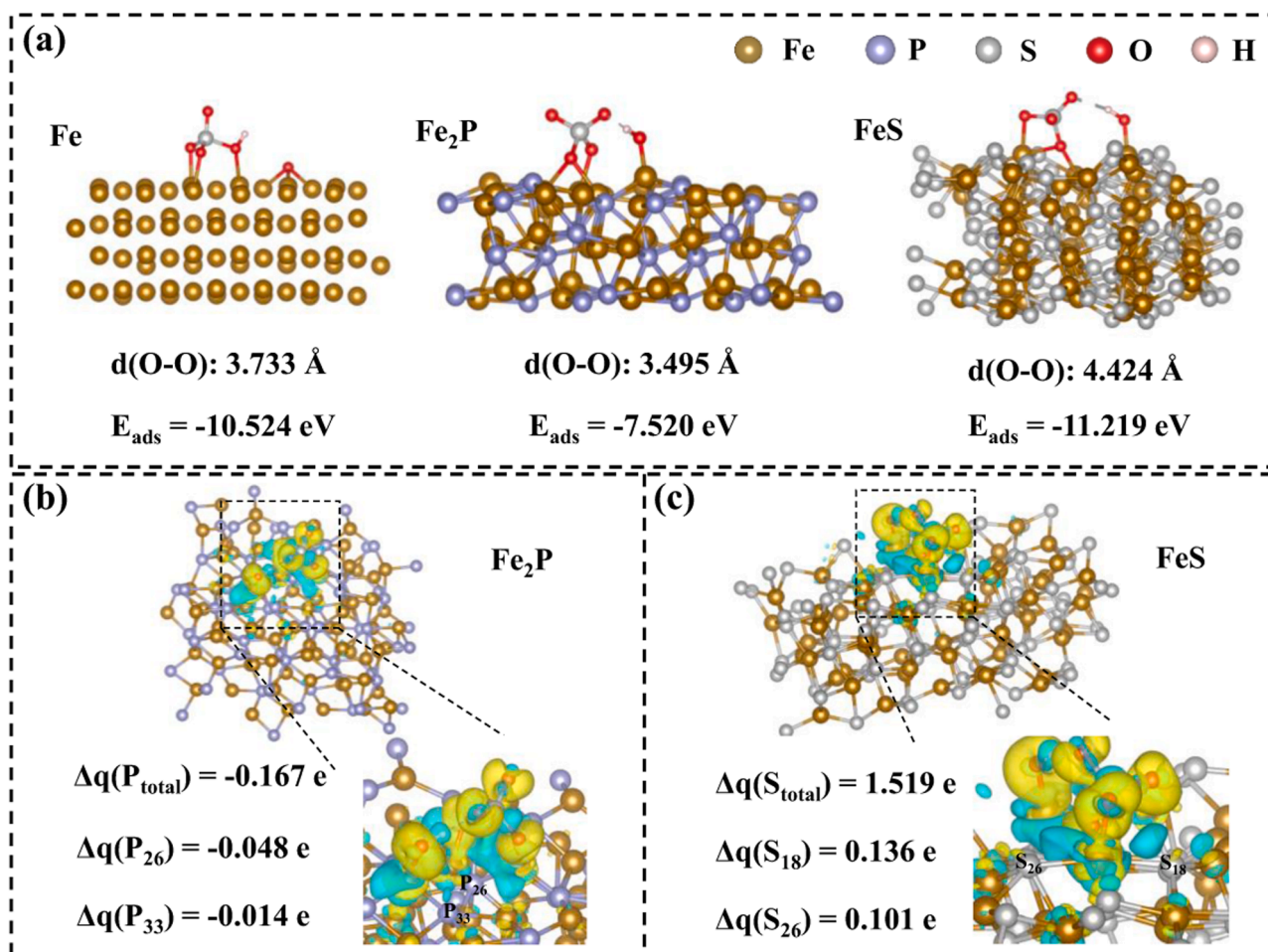


Fig. 5. Electronic structure analysis between PMS and catalysts. (a) Optimized configuration of PMS adsorbed on Fe, Fe<sub>2</sub>P, and FeS; (b-c) 3D charge density difference of PMS adsorbed on Fe<sub>2</sub>P and FeS (the yellow and sky blue isosurfaces denote electron accumulation and depletion, respectively.).

of the iron site to be closer to the Fermi level (Fig. S18). Therefore, we infer that the relatively electron-rich S has an electron transfer effect on the d-orbital of iron when it is introduced, thereby increasing its d-band center, while the electron-deficient P decreases its d-band center. Meanwhile, according to the d-band theory, the closer the electron density of the metal d orbital energy level is to the Fermi level, the more favorable it is to interact with the highest occupied molecular orbital and the lowest unoccupied molecular orbital of the surface adsorbate, which eventually leads to stronger adsorption [41]. Therefore, according to the above analysis, it can be concluded that compared with the relatively electron-deficient P-doped catalyst and the undoped catalyst, the electron-rich S-doped catalyst will increase the d-band center of the iron active site through the electron transfer effect, and finally increasing its adsorption performance to PMS. Furthermore, we calculated the adsorption energy of the catalyst to PMS to more intuitively understand their adsorption capacity for PMS. the adsorption energy (E<sub>ads</sub>) of FeS to PMS was calculated to be -11.219 eV, which was higher than that of the other two crystals. Therefore, it can be inferred that Fe@N/C-S has a strong binding ability to PMS, which leads to its superior activity. On the other hand, the adsorption energy of Fe for PMS is higher than that of Fe<sub>2</sub>P, suggesting that the catalytic activity of Fe@N/C is stronger than that of Fe@N/C-P, which is also consistent with the experimental results.

In addition, Bader charge analysis (Fig. S19) shows that the introduction of heteroatoms has a significant effect on the electron distribution of Fe active sites and further affects the valence distribution of Fe. We calculated the 3D charge density difference during PMS activation,

which can directly observe the electron transfer and redistribution between PMS and crystals [23]. Obviously, the yellow and sky blue regions can be seen at the active sites of PMS and Fe in the adsorption configuration, which indicates the effective activation of PMS on the iron sites (Fig. 5b-c and Fig. S20). Notably, some of the P and S atoms have different color regions around them, implying that they have different electron contributions when activating the PMS at the Fe site. The quantitative results of electron transfer were further obtained based on Bader charge analysis. Specifically, the P atom obtained 0.167 e from the Fe active site, while the S atom lost 1.519 e. This trend was consistent with the analysis results of XPS and PDOS. In other words, the electron-rich S atom can increase the d-band center of the Fe site, thereby enhancing its interaction with PMS, and at the same time providing electrons during the activation process, promote the mutual conversion between different Fe valence states, and improve the catalytic activity eventually, while the P atom, electron-withdrawing atom, slows down the activation of PMS at the Fe active sites.

### 3.6. Application potentials of Fe@N/C-S/PMS system

We conducted a batch of experiments to evaluate the application potential of Fe@N/C-S. First of all, several persistent organic pollutants were selected for the degradation in Fe@N/C-S/PMS system. It was found that they could be completely removed within 15 min, illustrating the strong oxidizing capacity of the system (Fig. 6a and Fig. S21). We then verified the effects of common anion and pH on SMX degradation. As shown in Fig. 6b, the degradation of SMX by Fe@N/C-S/PMS system

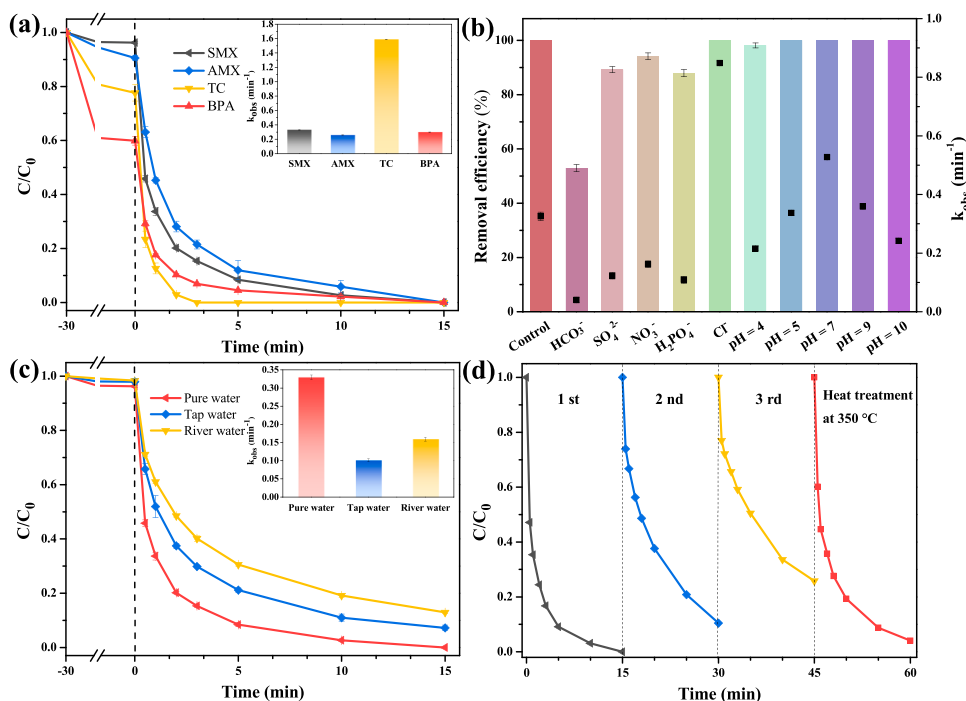


**Fig. 6.** Removal performance of Fe@N/C-S/PMS system under various conditions. (a) Removal of several typical pollutants by Fe@N/C-S/PMS system; (b) Effects of common anion and pH on SMX degradation; (c) SMX degradation in real waters; (d). Stability of Fe@N/C-S for SMX removal. Reaction conditions: [PMS] = 0.5 mM, [catalysts] = 0.05 g L<sup>-1</sup>, [SMX] = 10 mg L<sup>-1</sup>, [anion] = 200 mM, T = 25 °C, and initial pH = 7.4.

is almost unaffected in the wide pH range of 4–10 and in the presence of 200 mM common anion ( $\text{SO}_4^{2-}$ ,  $\text{NO}_3^-$ ,  $\text{H}_2\text{PO}_4^-$ , and  $\text{Cl}^-$ ), respectively. However, Fe@N/C does not show the ideal removal rate of SMX under the same conditions, which indicates that the doping of S and P can not only improve the activity efficiency of the catalyst, but also enhance the anti-interference ability. (Fig. S22). It is worth noting that  $\text{HCO}_3^-$  has a serious inhibitory effect on the degradation of SMX in the three systems, which may be caused by the buffering effect of high concentration of  $\text{HCO}_3^-$ . In order to confirm this view, we monitored the pH changes of the three systems during the reaction. It was found that in the presence of 200 mM  $\text{HCO}_3^-$ , the pH of the reaction system was always greater than 8, which was significantly higher than that without  $\text{HCO}_3^-$  (Fig. S23). We further examined the Zeta potential of the catalyst at different pH levels, and found that at high pH levels, the catalyst surface has a strong negative charge, making the electronegative  $\text{HSO}_5^-$  and SMX difficult to contact, resulting in a decrease in catalytic efficiency (Fig. S24) [42].

Additionally, we also examined the mineralization efficiency of SMX in Fe@N/C-S/PMS system (Fig. S25). The removal rate of total organic carbon reached 72.31% in 15 min, indicating that the system has a strong mineralization ability. Fe@N/C-S/PMS also shows high adaptability in different water environments (tap water and Xiangjiang River water, composition analysis shown in Table S9), and the removal efficiency of SMX can still reach more than 80% within 15 min (Fig. 6c). Stability is another important index to evaluate the application potential of the catalyst. At the third cycle, 75% degradation efficiency can still be achieved. More importantly, the catalytic activity can be restored when the degradation products on the surface of the catalyst were removed by heat treatment (Fig. 6d). We also tested the content of iron leached by the catalyst to verify its safety and harmlessness. After the first cycle, the leaching concentration of iron ions was 0.14 mg/L, which was lower than the current standards for drinking water quality in China (0.3 mg/L, GB 5749–2022). Meanwhile, we used 0.14 mg/L iron ion as a catalyst to activate PMS, and found that SMX only degraded about 3.4%, which indicated that the iron ions leach by the catalyst had no activation effect on PMS, that is, the possibility of iron ions participating in the formation of HV-Fe=O was excluded (Fig. S26). In addition to iron ions, the

leaching risk of P and S in the catalyst was also worth considering. we tested the content of P and S in the leaching solution. It can be found from Table S10 that the leaching amounts of P and S caused by the catalyst were 0.017 and 0.069 mg/L, respectively, which were almost negligible. Therefore, the leaching risk of heteroatoms (P and S) in this study can be ignored. In short, Fe@N/C-S/PMS system was highly adaptable to different water quality, and could efficiently and steadily abate various pollutants without secondary pollution.

### 3.7. Degradation pathways of SMX

The degradation intermediates of SMX in Fe@N/C-S/PMS system was detected by liquid chromatography-mass spectrometry (LC-MS), and proposed the possible degradation pathways. As shown in Fig. S27, the peak located at  $m/z = 253.9$  belongs to SMX, and its peak intensity decreased, indicating that SMX is gradually decomposed during the catalytic reaction. A total of 10 intermediates were detected throughout the oxidation process, and the corresponding mass charge ratios, chemical formulas and possible structures are shown in Table S11. Based on the intermediate structure and previous studies, we proposed three possible degradation pathways for SMX (Fig. 7).

The degradation of SMX mainly includes nitro substitution, N-S/C-S bond breaking, denitrification and desulfurization, which are mainly achieved by the oxidation of HV-Fe=O and  $^1\text{O}_2$ . Specifically,  $^1\text{O}_2$  is strongly electrophilic due to the empty 2p orbital, and the highly valence iron elements in HV-Fe=O also have a strong ability to seize electrons, which makes them easy to oxidize with electron rich sulfur-containing organic compounds [11,43]. In pathway I, HV-Fe=O and  $^1\text{O}_2$  produced by the system easily oxidized with electron-rich sulfonamide bonds, resulting in N-S bond breakage in SMX and the formation of P1 and P2 [44]. Subsequently, P2, on the one hand, under the reaction of hydrogen atom transfer of HV-Fe=O, will undergo nitro substitution to produce P4, and then P4 will be further desulfurized to produce P5, and on the other hand, it will undergo denitrification to produce P3 [12, 45]. For pathway II, the C-S bond between the sulfonyl group and the benzene ring is broken due to electrophilic attacks by HV-Fe=O and



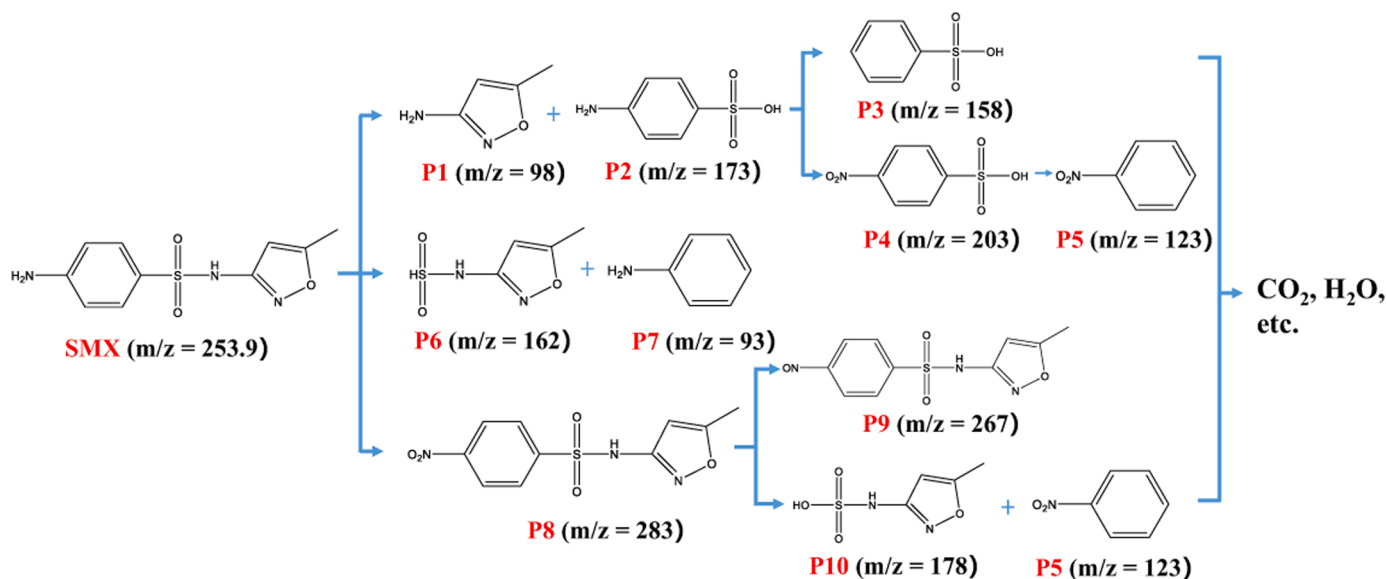


Fig. 7. Pathways proposed for SMX degradation in the Fe@N/C-S/PMS system.

$^1\text{O}_2$ , eventually forming P6 and P7. In pathway III, similar to the conversion of P2 to P5, the aniline group in SMX is easily oxidized by HV-Fe=O to P8. P8 can either be further generated into P5 and P10 by breaking the C-S bond similar to Pathway II, or it can be converted into P9 [46,47]. Finally, these intermediates would go on to be converted into other low molecular compounds and eventually into  $\text{H}_2\text{O}$  and  $\text{CO}_2$ .

#### 4. Conclusions

In summary, we constructed iron-based nanoparticle catalysts with heteroatoms anchored on nitrogen-doped carbon layers and systematically studied the role of P and S atoms in the activation of PMS by iron sites. Results showed that the S-doped catalysts achieved 100% removal of sulfamethoxazole (SMX) within 15 min with a normalized rate constant of  $130.4 \text{ min}^{-1} \text{ M}^{-1}$ , which was better than the recently reported advanced catalysts. EPR measurements and quenching experiments confirmed that  $^1\text{O}_2$  and HV-Fe=O were the main reactive species in the three catalyst-activated PMS systems. Further calculations show that the steady-state concentrations of HV-Fe=O and  $^1\text{O}_2$  are the highest in Fe@N/C/PMS and Fe@N/C-S/PMS systems, respectively. It is worth noting that the S-doped catalyst has superior anti-interference ability and can maintain excellent catalytic activity within wide pH range (4–10) and high concentration of interfering ions (200 mM). DFT calculations and experimental studies have elucidated the mechanism of heteroatoms doping-induced catalytic enhancement. The electron-rich S atom can provide electrons and affect the electron density distribution of Fe 3d orbital during PMS activation, thereby changing the valence distribution of Fe and enhancing the binding ability of Fe sites to PMS, resulting in excellent activation kinetics. The electron-deficient P atom was not favorable to PMS activation, and the rate constant was only  $53.83 \text{ min}^{-1} \text{ M}^{-1}$ . This study elaborates the electronic structure regulation and structure-activity relationship of metal centers in nanoparticles, which is helpful for the development of advanced catalysts.

#### CRediT authorship contribution statement

**Shaohua Wu:** Writing – review & editing, Writing – original draft, Investigation, Funding acquisition, Conceptualization. **Caiyu Luo:** Writing – original draft, Visualization, Writing – review & editing. **Juncong Zou:** Methodology, Software, Writing – review & editing. **Yan Lin:** Conceptualization, Investigation, Software, Writing – review & editing. **Shanying He:** Investigation, Methodology, Visualization.

**Chunping Yang:** Conceptualization, Funding acquisition, Project administration, Supervision, Writing – original draft, Writing – review & editing. **Jun Xie:** Writing – review & editing, Writing – original draft, Methodology, Investigation, Conceptualization.

#### Declaration of Competing Interest

The authors declare that they have no known competing financial interests or personal relationships that could have appeared to influence the work reported in this paper.

#### Data availability

Data will be made available on request.

#### Acknowledgements

This work was supported by the National Natural Science Foundation of China (Grant No.: 52270064, 52100081, 51978178 and 51521006), the Department of Science and Technology of Guangdong Province of China (Contract No.: 2024A1515010837, 2023A1515012062, 2022A1515010226, 2021A1515011797 and 2019A1515012044), the Science and Technology Innovation Program of Hunan Province of China (Contract No.: 2023RC3120), the Program for Innovative Research Teams of Guangdong Higher Education Institutes of China (Grant No.: 2021KCXTD043), the Key Laboratory of Petrochemical Pollution Control of Guangdong Higher Education Institutes (KLGHEI 2017KSYS004), and the Startup Fund of Guangdong University of Petrochemical Technology (Contract No.: 2020rc041 and 2018rc63).

#### Appendix A. Supporting information

Supplementary data associated with this article can be found in the online version at [doi:10.1016/j.apcatb.2024.124138](https://doi.org/10.1016/j.apcatb.2024.124138).

#### References

- [1] N. Hanna, A.J. Tamhankar, C.S. Lundborg, Antibiotic concentrations and antibiotic resistance in aquatic environments of the WHO Western Pacific and South-East Asia regions: a systematic review and probabilistic environmental hazard assessment, *Lancet Planet. Health* 7 (1) (2023) E45–E54, [https://doi.org/10.1016/S2542-5196\(22\)00254-6](https://doi.org/10.1016/S2542-5196(22)00254-6).

- [2] M. Kumar, S. Jaiswal, K.K. Sodhi, P. Shree, D.K. Singh, P.K. Agrawal, P. Shukla, Antibiotics bioremediation: perspectives on its ecotoxicity and resistance, *Environ. Int.* 124 (2019) 448–461, <https://doi.org/10.1016/j.envint.2018.12.065>.
- [3] D.G.J. Larsson, C.-F. Flach, Antibiotic resistance in the environment, *Nat. Rev. Microbiol.* 20 (5) (2022) 257–269, <https://doi.org/10.1038/s41579-021-00649-x>.
- [4] J. Wang, S. Wang, Microbial degradation of sulfamethoxazole in the environment, *Appl. Microbiol. Biotechnol.* 102 (8) (2018) 3573–3582, <https://doi.org/10.1007/s00253-018-8845-4>.
- [5] J. Wang, L. Chu, L. Wojnárovits, E. Takács, Occurrence and fate of antibiotics, antibiotic resistant genes (ARGs) and antibiotic resistant bacteria (ARB) in municipal wastewater treatment plant: An overview, *Sci. Total Environ.* 744 (2020) 140997, <https://doi.org/10.1016/j.scitotenv.2020.140997>.
- [6] G. Dong, B. Chen, B. Liu, L.J. Hounjet, Y. Cao, S.R. Stoyanov, M. Yang, B. Zhang, Advanced oxidation processes in microreactors for water and wastewater treatment: Development, challenges, and opportunities, *Water Res.* 211 (2022), <https://doi.org/10.1016/j.watres.2022.118047>.
- [7] J. Wang, S. Wang, Activation of persulfate (PS) and peroxymonosulfate (PMS) and application for the degradation of emerging contaminants, *Chem. Eng. J.* 334 (2018) 1502–1517, <https://doi.org/10.1016/j.cej.2017.11.059>.
- [8] J. Lee, U. von Gunten, J.-H. Kim, Persulfate-based advanced oxidation: critical assessment of opportunities and roadblocks, *Environ. Sci. Technol.* 54 (6) (2020) 3064–3081, <https://doi.org/10.1021/acs.est.9b07082>.
- [9] Y. Yan, Z. Wei, X. Duan, M. Long, R. Spinney, D.D. Dionysiou, R. Xiao, P.J. Alvarez, Merits and limitations of radical vs. nonradical pathways in persulfate-based advanced oxidation processes, *Environ. Sci. Technol.* 57 (33) (2023) 12153–12179, <https://doi.org/10.1021/acs.est.3c05153>.
- [10] W. Ren, C. Cheng, P. Shao, X. Luo, H. Zhang, S. Wang, X. Duan, Origins of electron-transfer regime in persulfate-based nonradical oxidation processes, *Environ. Sci. Technol.* 56 (1) (2022) 78–97, <https://doi.org/10.1021/acs.est.1c05374>.
- [11] Y. Wang, Y. Lin, S. He, S. Wu, C. Yang, Singlet oxygen: properties, generation, detection, and environmental applications, *J. Hazard. Mater.* 461 (2024), <https://doi.org/10.1016/j.jhazmat.2023.132538>.
- [12] Z. Wang, W. Qiu, S.-y. Pang, Q. Guo, C. Guan, J. Jiang, Aqueous iron(IV)-oxo complex: An emerging powerful reactive oxidant formed by iron(II)-based advanced oxidation processes for oxidative water treatment, *Environ. Sci. Technol.* 56 (3) (2022) 1492–1509, <https://doi.org/10.1021/acs.est.1c04530>.
- [13] S. Bhunia, A. Rana, S.G. Dey, A. Ivanchich, A. Dey, A designed second-sphere hydrogen-bond interaction that critically influences the O–O bond activation for heterolytic cleavage in ferric iron–porphyrin complexes, *Chem. Sci.* 11 (10) (2020) 2681–2695, <https://doi.org/10.1039/c9sc04388h>.
- [14] J. Xie, C. Yang, X. Li, S. Wu, Y. Lin, Generation and engineering applications of sulfate radicals in environmental remediation, 139659–139659, *Chemosphere* 339 (2023), <https://doi.org/10.1016/j.chemosphere.2023.139659>.
- [15] Y.Y. Mun, S. Lee, K. Kim, S. Kim, S. Lee, J.W. Han, J. Lee, Versatile strategy for tuning ORR activity of a single Fe-N<sub>4</sub> site by controlling electron-withdrawing/donating properties of a carbon plane, *J. Am. Chem. Soc.* 141 (15) (2019) 6254–6262, <https://doi.org/10.1021/jacs.8b13543>.
- [16] J. Zhang, Y. Zhao, C. Chen, Y.-C. Huang, C.-L. Dong, C.-J. Chen, R.-S. Liu, C. Wang, K. Yan, Y. Li, G. Wang, Tuning the coordination environment in single-atom catalysts to achieve highly efficient oxygen reduction reactions, *J. Am. Chem. Soc.* 141 (51) (2019) 20118–20126, <https://doi.org/10.1021/jacs.9b09352>.
- [17] S. Wang, Y. Liu, J. Wang, Peroxymonosulfate activation by Fe–Co–O-codoped graphite carbon nitride for degradation of sulfamethoxazole, *Environ. Sci. Technol.* 54 (16) (2020) 10361–10369, <https://doi.org/10.1021/acs.est.0c03256>.
- [18] S. Wang, Y. Liu, J. Wang, Iron and sulfur co-doped graphite carbon nitride (FeO<sub>y</sub>/S-g-C<sub>3</sub>N<sub>4</sub>) for activating peroxymonosulfate to enhance sulfamethoxazole degradation, *Chem. Eng. J.* 382 (2020) 122836, <https://doi.org/10.1016/j.cej.2019.122836>.
- [19] J. He, J. Tang, Z. Zhang, L. Wang, Q. Liu, X. Liu, Magnetic ball-milled FeS@biochar as persulfate activator for degradation of tetracycline, *Chem. Eng. J.* 404 (2021) 126997, <https://doi.org/10.1016/j.cej.2020.126997>.
- [20] N. Zheng, X. He, R. Hu, W. Guo, Z. Hu, Co-activation of persulfate by cation and anion from FeP for advanced oxidation processes, *Appl. Catal. B: Environ.* 298 (2021) 120505, <https://doi.org/10.1016/j.apcatb.2021.120505>.
- [21] J. Feng, M. Dou, Z. Zhang, F. Wang, Template-free synthesis of two-dimensional Fe/N codoped carbon networks as efficient oxygen reduction reaction electrocatalysts, *ACS Appl. Mater. Interfaces* 10 (43) (2018) 37079–37086, <https://doi.org/10.1021/acsami.8b13445>.
- [22] Y. He, H. Qin, Z. Wang, H. Wang, Y. Zhu, C. Zhou, Y. Zeng, Y. Li, P. Xu, G. Zeng, Fe-Mn oxycarbide anchored on N-doped carbon for enhanced Fenton-like catalysis: importance of high-valent metal-oxo species and singlet oxygen, *Appl. Catal. B: Environ.* 340 (2024), <https://doi.org/10.1016/j.apcatb.2023.123204>.
- [23] J. Zou, Y. Lin, C. Yang, Covalency triggers high catalytic activity of amorphous molybdenum oxides for oxidative desulfurization, *Sci. China Chem.* 66 (4) (2023) 1211–1220, <https://doi.org/10.1007/s11426-022-1534-8>.
- [24] Y. Wang, Y. Lin, C. Yang, S. Wu, X. Fu, X. Li, Calcination temperature regulates non-radical pathways of peroxymonosulfate activation via carbon catalysts doped by iron and nitrogen, *Chem. Eng. J.* 451 (2023) 138468, <https://doi.org/10.1016/j.cej.2022.138468>.
- [25] Y. Chen, R. Gao, S. Ji, H. Li, K. Tang, P. Jiang, H. Hu, Z. Zhang, H. Hao, Q. Qu, X. Liang, W. Chen, J. Dong, D. Wang, Y. Li, Corrigendum: Atomic-level modulation of electronic density at cobalt single-atom sites derived from metal–organic frameworks: enhanced oxygen reduction performance, *Angew. Chem. Int. Ed.* 61 (30) (2022) e202207879, <https://doi.org/10.1002/anie.202207879>.
- [26] X.-C. Feng, Z.-J. Xiao, H.-T. Shi, B.-Q. Zhou, Y.-M. Wang, H.-Z. Chi, X.-H. Kou, N.-Q. Ren, How nitrogen and sulfur doping modified material structure, transformed oxidation pathways, and improved degradation performance in peroxymonosulfate activation, *Environ. Sci. Technol.* 56 (19) (2022) 14048–14058, <https://doi.org/10.1021/acs.est.2c04172>.
- [27] S. Wu, H. Liu, C. Yang, X. Li, Y. Lin, K. Yin, J. Sun, Q. Teng, C. Du, Y. Zhong, High-performance porous carbon catalysts doped by iron and nitrogen for degradation of bisphenol F via peroxymonosulfate activation, *Chem. Eng. J.* 392 (2020) 123683, <https://doi.org/10.1016/j.cej.2019.123683>.
- [28] X. Fu, Y. Lin, C. Yang, S. Wu, Y. Wang, X. Li, Peroxymonosulfate activation via CoP nanoparticles confined in nitrogen-doped porous carbon for enhanced degradation of sulfamethoxazole in wastewater with high salinity, *J. Environ. Chem. Eng.* 10 (3) (2022) 107734, <https://doi.org/10.1016/j.jece.2022.107734>.
- [29] S. Wu, Z. Yang, Z. Zhou, X. Li, Y. Lin, J.J. Cheng, C. Yang, Catalytic activity and reaction mechanisms of single-atom metals anchored on nitrogen-doped carbons for peroxymonosulfate activation, *J. Hazard. Mater.* 459 (2023) 132133, <https://doi.org/10.1016/j.jhazmat.2023.132133>.
- [30] C. Luo, Y. Lin, Y. Zhang, S. Zhang, S. Tong, S. Wu, C. Yang, S-scheme heterojunction between MOFs and Ag<sub>3</sub>PO<sub>4</sub> leads to efficient photodegradation of antibiotics in swine wastewater, *Sep. Purif. Technol.* 320 (2023) 124052, <https://doi.org/10.1016/j.seppur.2023.124052>.
- [31] B. D'Aurèaux, M.B. Toledano, ROS as signalling molecules: mechanisms that generate specificity in ROS homeostasis, *Nat. Rev. Mol. Cell Biol.* 8 (10) (2007) 813–824, <https://doi.org/10.1038/nrm2256>.
- [32] Z. Wang, W. Wang, J. Wang, Y. Yuan, Q. Wu, H. Hu, High-valent iron-oxo species mediated cyclic oxidation through single-atom Fe-N<sub>6</sub> sites with high peroxymonosulfate utilization rate, *Appl. Catal. B: Environ.* 305 (2022) 121049, <https://doi.org/10.1016/j.apcatb.2021.121049>.
- [33] Z. Wang, J. Jiang, S. Pang, Y. Zhou, C. Guan, Y. Gao, J. Li, Y. Yang, W. Qiu, C. Jiang, Is sulfate radical really generated from peroxydisulfate activated by iron (II) for environmental decontamination? *Environ. Sci. Technol.* 52 (19) (2018) 11276–11284, <https://doi.org/10.1021/acs.est.8b02266>.
- [34] A.L. Boreen, W.A. Arnold, K. McNeill, Photochemical fate of sulfa drugs in the aquatic environment: sulfa drugs containing five-membered heterocyclic groups, *Environ. Sci. Technol.* 38 (14) (2004) 3933–3940, <https://doi.org/10.1021/es0353053>.
- [35] Y. Mao, J. Liang, F. Ji, H. Dong, L. Jiang, Q. Shen, Q. Zhang, Accelerated degradation of pharmaceuticals by ferrous ion/chlorine process: Roles of Fe(IV) and reactive chlorine species, *Sci. Total Environ.* 787 (2021) 147584, <https://doi.org/10.1016/j.scitotenv.2021.147584>.
- [36] Y. Yao, C. Wang, X. Yan, H. Zhang, C. Xiao, J. Qi, Z. Zhu, Y. Zhou, X. Sun, X. Duan, J. Li, Rational regulation of Co–N–C coordination for high-efficiency generation of <sup>1</sup>O<sub>2</sub> toward nearly 100% selective degradation of organic pollutants, *Environ. Sci. Technol.* 56 (12) (2022) 8833–8843, <https://doi.org/10.1021/acs.est.2c00706>.
- [37] H. Li, C. Shan, B. Pan, Fe(III)-doped g-C<sub>3</sub>N<sub>4</sub> mediated peroxymonosulfate activation for selective degradation of phenolic compounds via high-valent iron-oxo species, *Environ. Sci. Technol.* 52 (4) (2018) 2197–2205, <https://doi.org/10.1021/acs.est.7b05563>.
- [38] J. Zou, Y. Lin, S. Wu, Y. Zhong, C. Yang, Molybdenum dioxide nanoparticles anchored on nitrogen-doped carbon nanotubes as oxidative desulfurization catalysts: Role of electron transfer in activity and reusability, *Adv. Funct. Mater.* 31 (22) (2021) 2100442, <https://doi.org/10.1002/adfm.202100442>.
- [39] J. Zou, S. Wu, Y. Lin, S. He, Q. Niu, X. Li, C. Yang, Electronic phosphide-support interactions in carbon-supported molybdenum phosphide catalysts derived from metal–organic frameworks, *Nano Lett.* 23 (23) (2023) 10955–10963, <https://doi.org/10.1021/acs.nanolett.3c03217>.
- [40] S. Jiao, X. Fu, H. Huang, Descriptors for the evaluation of electrocatalytic reactions: d-band theory and beyond, *Adv. Funct. Mater.* 32 (4) (2022) 2107651, <https://doi.org/10.1002/adfm.202107651>.
- [41] Y. Zhang, X. Chen, C. Liang, L. Yin, Y. Yang, Reconstructing the coordination environment of single atomic Fe-catalysts for boosting the Fenton-like degradation activities, *Appl. Catal. B: Environ.* 315 (2022) 121536, <https://doi.org/10.1016/j.apcatb.2022.121536>.
- [42] J.-C.E. Yang, B. Yuan, H.-J. Cui, S. Wang, M.-L. Fu, Modulating oxone-MnO<sub>x</sub>/silica catalytic systems towards ibuprofen degradation: insights into system effects, reaction kinetics and mechanisms, *Appl. Catal. B: Environ.* 205 (2017) 327–339, <https://doi.org/10.1016/j.apcatb.2016.12.046>.
- [43] A.G. Mojarad, S. Zakavi, Simple low cost porphyrinic photosensitizers for large scale chemoselective oxidation of sulfides to sulfoxides under green conditions: targeted protonation of porphyrins, *Catal. Sci. Technol.* 8 (3) (2018) 768–781, <https://doi.org/10.1039/C7CY02308A>.
- [44] J. Du, W. Guo, H. Wang, R. Yin, H. Zheng, X. Feng, D. Che, N. Ren, Hydroxyl radical dominated degradation of aquatic sulfamethoxazole by Fe<sup>0</sup>/bisulfite/O<sub>2</sub>: kinetics, mechanisms, and pathways, *Water Res.* 138 (2018) 323–332, <https://doi.org/10.1016/j.watres.2017.12.046>.
- [45] X. Wang, W. Li, Y. Wang, L. Yang, J. Zhang, G. Zhao, Q. Zhao, Efficient removal of sulfamethoxazole by biomass phosphorus-derived Cu<sub>3</sub>P/biochar catalyst combined with persulfate, *Sep. Purif. Technol.* 326 (2023) 124768, <https://doi.org/10.1016/j.seppur.2023.124768>.
- [46] Y. Bao, W.-D. Oh, T.-T. Lim, R. Wang, R.D. Webster, X. Hu, Elucidation of stoichiometric efficiency, radical generation and transformation pathway during catalytic oxidation of sulfamethoxazole via peroxymonosulfate activation, *Water Res.* 151 (2019) 64–74, <https://doi.org/10.1016/j.watres.2018.12.007>.
- [47] D.T. Oyekunle, E.A. Gendy, J. Iftikhar, Z. Chen, Heterogeneous activation of persulfate by metal and non-metal catalyst for the degradation of sulfamethoxazole: a review, *Chem. Eng. J.* 437 (2022) 135277, <https://doi.org/10.1016/j.cej.2022.135277>.